(Received 3 November 2025, Accepted 9 December 2025, Scheduled 25 January 2026)

Characterization of Complex Permittivity Using Microwave Diffraction of Spheres

Elio Samara, Jean-Michel Geffrin, and Amelie Litman*

Aix Marseille University, CNRS, Centrale Med, Institut Fresnel, Marseille, France

ABSTRACT: The determination of the complex permittivity of materials is a fundamental aspect of experimental electromagnetics. This study introduces a method that estimates the complex permittivity by comparing the measured bistatic field diffracted by spherical samples in an anechoic chamber with fields computed using Mie theory. The approach is applied to a molded PMMA sphere and to two 3D-printed materials (Clear Resin V4.1 and Rigid 10 K) over the 2–18 GHz band. The retrieved permittivity values show excellent agreement with reference data for PMMA and enable reliable characterization of low-loss 3D-printed materials, with uncertainties quantified from both experimental and numerical contributions. These results confirm the effectiveness of microwave-diffraction-based characterization and highlight promising perspectives for future investigations on an even larger frequency band.

1. INTRODUCTION

Characterizing the complex permittivity of materials is essential for many electromagnetic applications, as inaccuracies can significantly impact radar signatures, wave propagation, and device performance. Conventional methods for measuring permittivity in the microwave domain, such as those based on resonators, cavities, transmission lines, or waveguides, provide accurate results but also have limitations, including narrow operational frequency bands, sensitivity to sample preparation, and constraints related to the ratio between the sample volume and the cavity volume [1–7]. To overcome these limitations, we propose a method based on microwave diffraction to determine the permittivity of objects, including those manufactured by 3D printing.

This approach relies on measurements performed in an anechoic chamber and offers the advantage of characterizing objects of virtually any size, as long as the diameter of the sphere enclosing the object must not be too small relative to the wavelength used. In this study, we consider targets for which the enclosing sphere has a diameter d such that $d > \lambda/4$ in order to keep the scattered field level above the current noise floor of our measuring device. Unlike cavity-based or waveguide-based techniques, our method, therefore, does not require standardized sample geometries or delicate machining of the samples, and it can be extended to other geometries provided that they are known a priori. In addition to this geometric flexibility, the proposed approach provides broadband characterization, as it operates over the 2–18 GHz band and can be extended up to 40 GHz with the current experimental system. Furthermore, the full acquisition and processing chain is relatively fast: the complete measurement procedure requires approximately two hours, making the method suitable for routine material characterization.

* Corresponding author: Amelie Litman (amelie.litman@fresnel.fr).

Similar approaches relying on scattering phenomenon have been proposed, such as the ones in [8–10], which exploits Mie-theory comparisons to extract the permittivity of sub-resonant dielectric spheres from the measured scattered field. In these works, some limitations are imposed: either the scattered field is acquired for a single bistatic angle [8], or the radius of the sphere is also chosen to be unknown [8], or the permittivity is constant over the considered frequency range [8, 10], or only the two first multipolar terms of the Mie series are computed [9].

In the present work, as in our previous study [11], we assume firstly that the sample geometry is known, secondly that we acquire the scattered field at each frequency for almost all bistatic angles, with the exception of a forbidden angular zone in the backward direction, and thirdly that the permittivity can vary as a function of frequency. This contribution expands the scope of our previous study to larger objects, lower frequencies, and additive-manufactured samples. It benefits from the new MIMOSA (Multi-Incidences Multi-Orientations Scattering Analyzer) measurement system, which offers enhanced angular bistatic coverage and improved data processing capabilities. In addition, our new uncertainty estimation technique integrates both experimental and geometrical errors contributions.

The methodology is described as follows. In parallel with the measurements, the field diffracted by the sphere for different permittivity values is computed using Mie series [12]. The complex permittivity is estimated by minimizing, in a least-square sense, the discrepancy between measured and simulated fields, as detailed in Section 2. For each sample, the complex permittivity $(\varepsilon' + j\varepsilon'')$, the loss tangent $\tan(\delta)$ and the refractive index $(n' + j\kappa)$ are estimated at each frequency. Uncertainties are also computed taking into account at the same time measurement and geometrical errors. Section 3 presents the results over the 2–18 GHz band obtained for three types of spheres fab-

ricated by additive manufacturing: a molded PMMA sphere and two 3D-printed materials (Clear Resin V4.1 and Rigid 10 K). Conclusions and perspectives follow in Section 4.

2. MATERIALS AND METHODS

The diffraction by an object is directly influenced by the electromagnetic properties of the material composing it, making the analysis of diffracted fields a valuable tool for extracting information about targets. Among the various types of possible targets, this study focuses exclusively on homogeneous spherical samples. We also assume that the materials are non-magnetic and isotropic. Under these conditions, the diffracted field depends on the following parameters: the radius of the sphere, the position of its center, the real part (ε') and imaginary part (ε'') of its permittivity, the frequency and polarization of the incident wave. The use of Mie series eliminates potential numerical errors; however, geometric inaccuracies may arise from the additive manufacturing of the spheres, which can affect the measurements.

2.1. Measurements and Calibration

To perform these diffraction measurements, the sample is placed on a polystyrene support in our anechoic chamber, equipped with two antennas, a transmitter, and a receiver that could move independently. The receiving antenna performed a circular scan around the sphere, with an angular sector excluded due to mechanical constraints ($\phi_s = -180°$, $\phi_r = -146° : 2° : 146°$). To obtain the diffracted field of the sphere, two separate measurements are subtracted: the total field, with the sphere, and the incident field, without the sphere. Acquiring these two measurements, along with the calibration measurement, required approximately 2 hours.

During these measurements, the transmitting antenna radiates an electromagnetic wave over the frequency range of 2 to 18 GHz. For each frequency, measurements are performed at all accessible positions of the receiving antenna (Fig. 1). This process provides the angular characterization of the diffracted field at each frequency. The measurements are calibrated against a reference measurement: that of a metallic sphere (with diameter $d = 35$ mm), which is compared to the calculation of the Mie theory for such a sphere. This calibration procedure normalizes the measurement to what would be obtained for an excitation with an amplitude of 1 V/m and 0° phase at the center of the object. The measured field is then processed to eliminate drift errors as explained in [13].

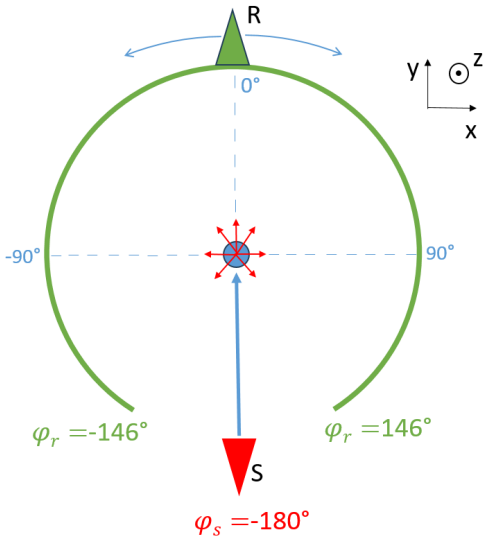

FIGURE 1. Representation of the receiving antenna path (R in green), around the sphere with the position of the source antenna (S in red).

2.2. Permittivity Estimation

This calibrated and corrected field is compared to a simulated field. For each candidate pair $(\varepsilon', \varepsilon'')$, or equivalently for each $\varepsilon = \varepsilon' + j\varepsilon''$, a difference metric, denoted as the cost function F^c, is evaluated at each frequency to quantify the difference between the measured field E_{meas} and simulated field E_{sim} Eq. (1).

$$F^c(\varepsilon) = \sum_{\phi_r} |E_{meas}(\phi_r) - E_{sim}(\phi_r, \varepsilon)|^2 \qquad (1)$$

When little or no prior information about the material is available, the first step consists of defining a plausible search space for the complex permittivity, as there can be several local minima. An initial coarse exploration is therefore performed, scanning ε' and ε'' over a large range with a step of 0.1 for both parameters (Fig. 2). The minimum value of this cost function map is then identified to determine the estimated values of ε'_0 and ε''_0, that is, the values for which the simulated fields best match the measured fields with respect to this step grid.

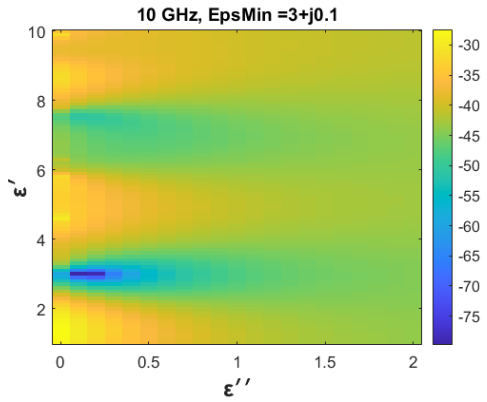

FIGURE 2. Variation of the cost function F^c (in dB) over a wide interval of ε' and ε'' with a step size of 0.1 for each parameter, at 10 GHz for the ClearResin V4.1 sphere.

To refine the permittivity value, using $\varepsilon'_0 + j\varepsilon''_0$ as the starting guess, a local optimization is then carried out using the Nelder-Mead algorithm (fminsearch in MATLAB), which further refines the estimate by minimizing the cost function around the previously identified minimum. To ensure rigorous minimization, the convergence tolerance was set to 10^{-4} , meaning that the algorithm terminates only when the successive variations in permittivity, $\Delta\varepsilon_{\text{num}}$, become smaller than 10^{-4}

$$\Delta\varepsilon_{\text{num}} = |\varepsilon_{k+1} - \varepsilon_k| < 10^{-4} \qquad (2)$$

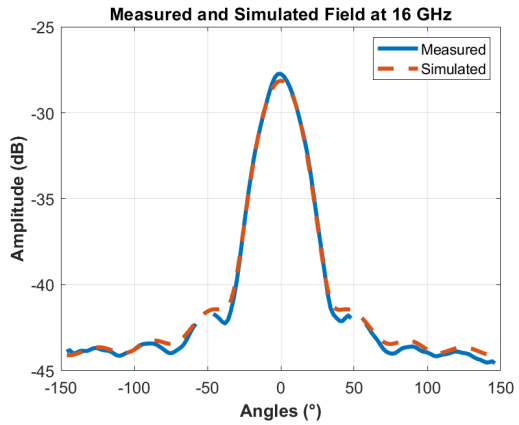

FIGURE 3. Comparison of the amplitude of simulated and measured fields for a 35 mm diameter metallic sphere.

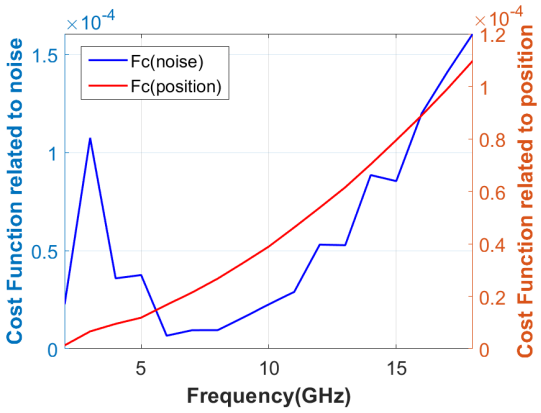

FIGURE 4. Evolution of cost functions related to noise and positioning vs frequency for a 35 mm diameter metallic sphere.

Once $\varepsilon_{\min}$ is estimated, we can compute the associated loss tangent and refractive index

$$\tan(\delta_{\min}) = \varepsilon''_{\min}/\varepsilon'_{\min} \quad (3)$$

$$n_{\min} = n'_{\min} + j\kappa_{\min} = \sqrt{\varepsilon_{\min}} \quad (4)$$

2.3. Uncertainty Estimation

The final precision of the permittivity estimation thus depends on several factors. The initial search grid is chosen here with a step size of 0.1 for both ε' and ε'', allowing a first approximation of these parameters. Then, through refinement with the fminsearch function, the precision can be improved to $\Delta\varepsilon_{\text{num}}$. However, since these permittivity estimates rely on the comparison between measured and simulated fields, the accuracy of the experimental measurements directly affects the estimated values. Therefore, the final precision is limited by experimental uncertainties, such as measurement noise and sphere positioning errors. Geometric fabrication errors of the spheres, however, are neglected. The overall uncertainty in the estimated permittivity can thus be expressed as the sum of numerical and experimental uncertainties: $\pm\,(\Delta\varepsilon_{\text{num}} + \Delta\varepsilon_{\text{exp}})$.

Thanks to our alignment technique, the uncertainty in the sphere's position can be estimated at ± 0.2 mm from the ideal position. The impact of this uncertainty is assessed using the

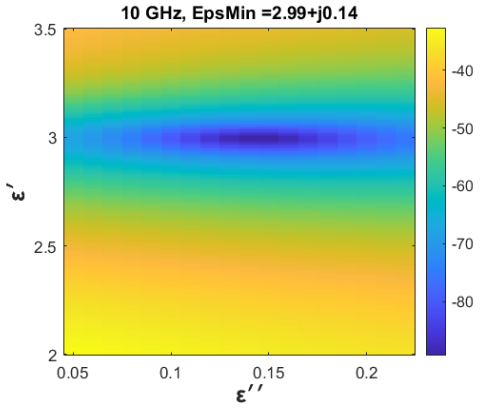

FIGURE 5. Variation of the cost function (in dB) over a refined interval of ε' and ε'' with a step size of 0.01 for each parameter.

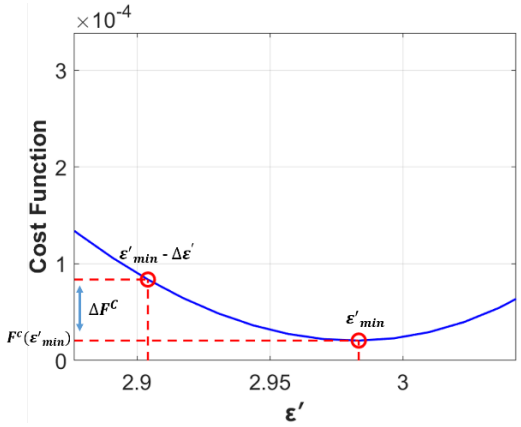

FIGURE 6. Estimation of the error on the real part of the permittivity as a function of the uncertainty on the cost function.

cost function $F^c_{position}$, which compares the simulated field for a sphere exactly centered to that obtained with a 0.2 mm offset. Similarly, the uncertainty due to measurement noise is evaluated via the cost function F^c_{noise}, which compares the measured field with the simulated field for a metallic sphere (Fig. 3).

The cost function related to position $F^c_{position}$ and the one related to noise F^c_{noise} are presented in Fig. 4 as a function of frequency. These two contributions are then summed at each frequency to form:

$$\Delta F^c = F^c_{position} + F^c_{noise} \quad (5)$$

The measurement uncertainty, $\Delta\varepsilon_{\text{exp}}$, is then estimated using the following equation

$$F^c(\varepsilon_{\min} \pm \Delta\varepsilon_{\text{exp}}) \leq F^c(\varepsilon_{\min}) + \Delta F^c \quad (6)$$

To estimate the uncertainty in permittivity, we propagate the error calculated in the cost function. For this, we first recompute the cost function F^c over a small range around $\varepsilon_{\min}$ with a step size of 0.01 for both the real and imaginary parts (Fig. 5). As illustrated in Fig. 6, which corresponds to the 1D-slice of Fig. 5 at $\varepsilon'' = \varepsilon''_{\min}$, we identify the minimum of the cost function and then perturb this minimum cost function value by its associated uncertainty $F^c + \Delta F^c$. By projecting onto the abscissa axis, we can determine the corresponding change in per-

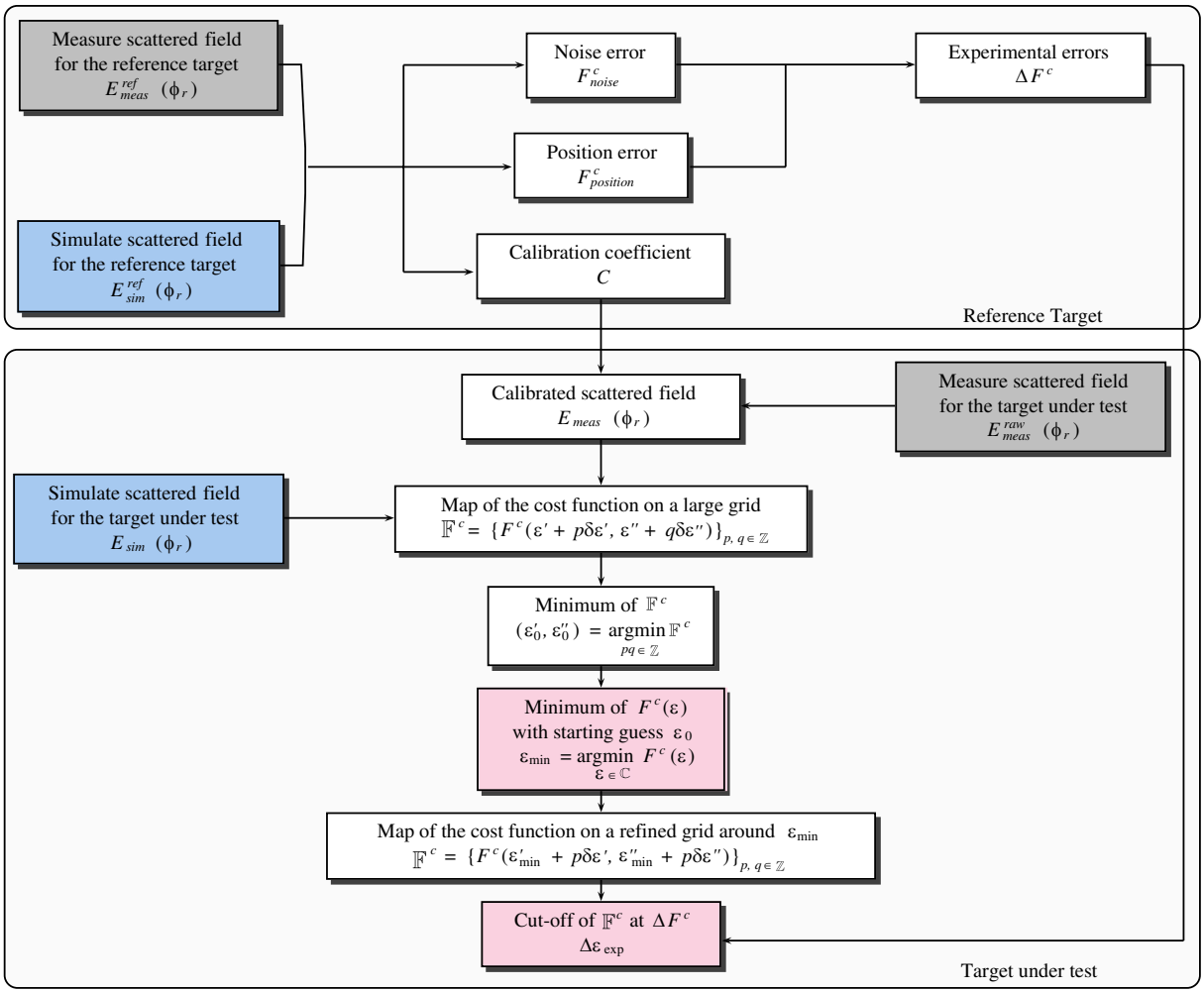

FIGURE 7. Flowchart summarizing the full process.

mittivity, denoted $\Delta\varepsilon'_{\text{exp}}$. This approach provides an estimate of the error on the real part of the permittivity resulting from the uncertainty in the cost function. The same approach is used to estimate the error in the imaginary part of the permittivity $\Delta\varepsilon''_{\text{exp}}$ from the cut at $\varepsilon' = \varepsilon'_{\text{min}}$.

From the uncertainties associated with ε' and ε'', the error on the loss tangent and the refractive index are calculated by applying the propagation of the uncertainty according to Eqs. (7)–(9) [14].

$$\Delta(\tan\delta) = \sqrt{\left|\frac{\varepsilon''}{(\varepsilon')^2}\right|^2 (\Delta\varepsilon')^2 + \left|\frac{1}{\varepsilon'}\right|^2 (\Delta\varepsilon'')^2} \tag{7}$$

$$\Delta n' = \frac{1}{4n'}\sqrt{\left(\frac{\varepsilon'}{|\varepsilon|}+1\right)^2 (\Delta\varepsilon')^2 + \left(\frac{\varepsilon''}{|\varepsilon|}\right)^2 (\Delta\varepsilon'')^2} \tag{8}$$

$$\Delta\kappa = \frac{1}{4\kappa}\sqrt{\left(\frac{\varepsilon'}{|\varepsilon|}-1\right)^2 (\Delta\varepsilon')^2 + \left(\frac{\varepsilon''}{|\varepsilon|}\right)^2 (\Delta\varepsilon'')^2} \tag{9}$$

2.4. Data Processing Flowchart

To summarize, the flowchart presented in Fig. 7 provides an overview of the full processing chain from measurement to permittivity estimation. It involves several key steps: (i) acquisition of total and incident field measurements over the full angular range to obtain the raw scattered field E^{raw}_{meas}; (ii) correction and calibration of the diffracted measured field; (iii) comparison of the calibrated field E_{meas} with Mie-theory simulations E_{sim} through the cost function F^c evaluated over a wide range of permittivities; (iv) a two-stage minimization, consisting first of a local refinement to obtain a crude estimation ε_0 of the minimum, followed by an optimization using the Nelder-Mead algorithm, to identify the permittivity ε_{min} that minimizes the cost function; and finally (v) propagation of numerical and experimental uncertainties to determine the confidence intervals on ε', ε'', loss tangent, and refractive indexes.

3. RESULTS AND DISCUSSION

This procedure was applied to the three materials presented in this article: one molded sphere and two 3D-printed spheres.

Firstly, to validate the technique, the measurement was performed on a molded polymethyl methacrylate (PMMA) sphere with a diameter of $d = 38.1$ mm. This material has also been studied in other works, where similar values were obtained (Fig. 8) [11, 15].

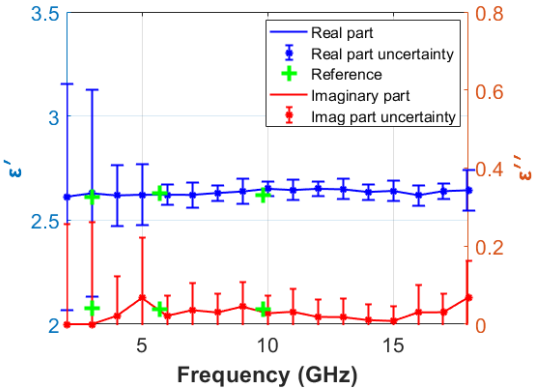

FIGURE 8. Real and imaginary parts of the permittivity of PMMA as a function of frequency, with error bars.

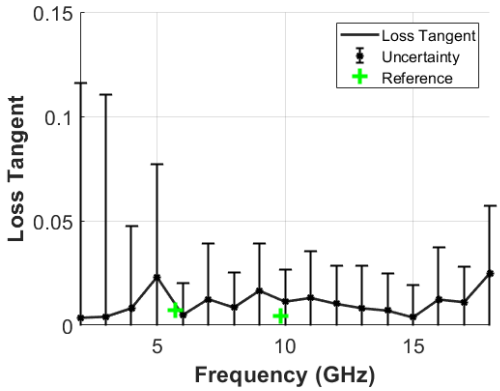

FIGURE 9. Loss tangent of PMMA as a function of frequency, with error bars.

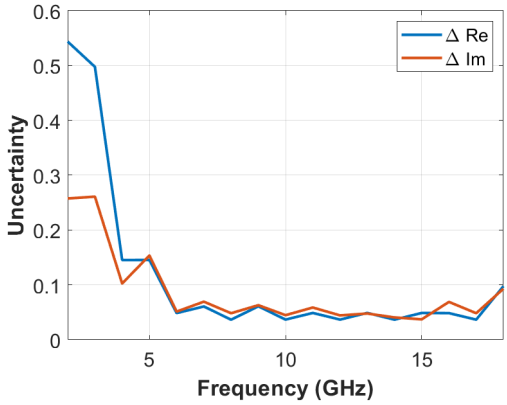

FIGURE 10. Uncertainty in permittivity estimation as a function of the frequency for both the real and imaginary parts, for a PMMA sphere.

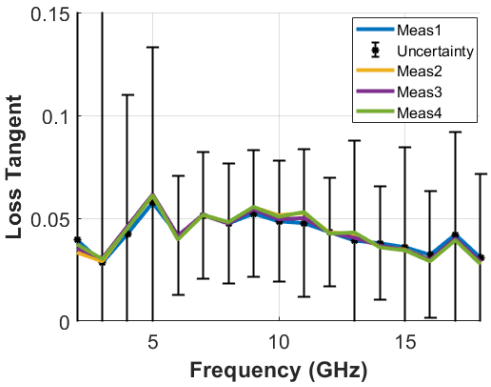

FIGURE 11. Loss tangent of the ClearResin V4.1 for four different measurements, with error bars.

The permittivity and loss tangent estimates of polymethyl methacrylate are presented in Figs. 8 and 9, showing the real and imaginary parts over the frequency range of 2 to 18 GHz with error bars and reference values from the literature [16]. The uncertainty of these estimations was calculated for each frequency (Fig. 10), based on both numerical and experimental uncertainties, which vary with frequency. These uncertainties are represented as error bars on the permittivity curves. Here, the ratio between the wavelength and the sphere diameter plays a key role in the magnitude of these uncertainties, particularly at low frequencies. As the sphere diameter becomes small relative to the wavelength, the error increases as the level of the scattered field is getting closer to the noise floor of the acquisition system. In our case, the minimum frequency considered is 2 GHz, corresponding to a wavelength of 150 mm. Although the recommended condition $d > \lambda/4$ is satisfied, the results at 2 and 3 GHz still show noticeably larger deviations compared with higher frequencies, highlighting the practical importance of this constraint.

Subsequently, two 3D-printed materials were measured: Clear Resin V4.1 and Rigid 10 K (Formlabs, $d = 35$ mm). The permittivity values estimated at 10 GHz are presented in Table 1.

The results show that the values obtained for PMMA are in very good agreement with those reported in the literature, confirming the reliability of the method. Clear Resin V4.1 and Rigid 10 K exhibit slightly higher (ε') than PMMA. In terms of losses, Clear Resin V4.1 shows higher ε'' and $\tan\delta$, while Rigid 10 K remains close to PMMA with low dielectric losses.

TABLE 1. Permittivity and refractive index estimation at 10 GHz, including uncertainties.

Materials	PMMA	Clear Resin V4.1	Rigid 10 k
$\varepsilon' \pm \Delta\varepsilon'$	2.64 ± 0.04	3.00 ± 0.08	3.35 ± 0.04
$\varepsilon'' \pm \Delta\varepsilon''$	0.03 ± 0.05	0.15 ± 0.09	0.06 ± 0.04
$\tan(\delta) \pm \Delta\tan(\delta)$	0.01 ± 0.02	0.05 ± 0.03	0.02 ± 0.01
$n' \pm \Delta n'$	1.62 ± 0.01	1.73 ± 0.02	1.83 ± 0.01
$\kappa \pm \Delta\kappa$	0.01 ± 0.02	0.04 ± 0.03	0.02 ± 0.01

To verify the repeatability of the estimation process, multiple measurements were performed on the same material by rotating the polystyrene mat support around its own axis at an angle ϕ_o, corresponding to the angle of self-rotation of the object. Four measurements were carried out, each corresponding to a different orientation of the support, with a 90° rotation step. The results are presented in Fig. 11, where the loss tangent is shown, reflecting the estimated real and imaginary parts of the permittivity. In particular, the values obtained from the

four different orientations are in close agreement, with variations significantly smaller than the associated error bars at each frequency. This consistency indicates accurate positioning of the sphere at the center of the support and the small effect of the imperfect sphericity of the sample. Regarding error bars at low frequencies (below 5 GHz), the relatively high uncertainties already mentioned above arise from the small level of the diffracted field for such a small object (see the small ratio between the wavelength and the diameter of the sphere). To reduce these uncertainties, one would need to use a larger sphere made of the same material.

4. CONCLUSION

In this study, a method for determining the complex permittivity of solid materials based on the exploitation of microwave diffraction by spheres is proposed. By minimizing the cost function, the complex permittivity values for PMMA, ClearV4.1, and Rigid 10 k were estimated, with associated uncertainties that partially account for experimental and numerical errors. The results confirmed the reliability of the proposed approach, particularly for materials made using 3D printing. The method performed consistently well across most frequencies; however, at lower frequencies, its accuracy was constrained by the low level of scattered measured fields. The precision of the permittivity evaluation at low frequencies can be improved using a larger sphere. The measurements presented in this work were conducted between 2 GHz and 18 GHz. However, as previously mentioned, the experimental setup is capable of operating up to 40 GHz, which opens perspectives for future investigations at higher frequencies, where material characterization and scattering phenomena may reveal additional insights. Incorporating models such as ohmic model, Drude-Lorentz model, and Kramers-Kronig relationship, during the retrieval step to link the real and imaginary parts of the permittivity also constitutes an interesting perspective for future work.

ACKNOWLEDGEMENT

This project is funded by the "France 2030" investment plan managed by the French National Research Agency (ANR-21-ESRE-0002). It also received funding from the ERC Advanced Grant DUST2PLANET (No. 240676) and the Institut Origines — From Planets to Life at Aix-Marseille University.

AUTHOR CONTRIBUTIONS

All authors contributed to the development of the methodology. E.S. developed the data processing tools, performed the data analysis, produced all figures, and drafted the manuscript. J.-M.G. performed the experimental measurements and supervised the data processing and analysis. A.L. supervised the project, contributed to the interpretation of the results, and revised the manuscript together with J.-M.G. All authors reviewed and approved the final manuscript.

REFERENCES

[1] Ba, D. and P. Sabouroux, "EpsiMu, a toolkit for permittivity and permeability measurement in microwave domain at real time of all materials: Applications to solid and semisolid materials," *Microwave and Optical Technology Letters*, Vol. 52, No. 12, 2643–2648, 2010.

[2] Akhtar, M. J., L. E. Feher, and M. Thumm, "A waveguide-based two-step approach for measuring complex permittivity tensor of uniaxial composite materials," *IEEE Transactions on Microwave Theory and Techniques*, Vol. 54, No. 5, 2011–2022, 2006.

[3] Parkash, A., J. K. Vaid, and A. Mansingh, "Measurement of dielectric parameters at microwave frequencies by cavity-perturbation technique," *IEEE Transactions on Microwave Theory and Techniques*, Vol. 27, No. 9, 791–795, 1979.

[4] Peng, Z., J.-Y. Hwang, and M. Andriese, "Maximum sample volume for permittivity measurements by cavity perturbation technique," *IEEE Transactions on Instrumentation and Measurement*, Vol. 63, No. 2, 450–455, 2014.

[5] Nicolson, A. M. and G. F. Ross, "Measurement of the intrinsic properties of materials by time-domain techniques," *IEEE Transactions on Instrumentation and Measurement*, Vol. 19, No. 4, 377–382, 1970.

[6] Gorriti, A. G. and E. C. Slob, "A new tool for accurate *S*-parameters measurements and permittivity reconstruction," *IEEE Transactions on Geoscience and Remote Sensing*, Vol. 43, No. 8, 1727–1735, 2005.

[7] Weir, W. B., "Automatic measurement of complex dielectric constant and permeability at microwave frequencies," *Proceedings of the IEEE*, Vol. 62, No. 1, 33–36, 1974.

[8] Lippoldt, M. and J. Hesselbarth, "Characterization of subresonant dielectric spheres by millimeter-wave scattering measurements," *Sensors*, Vol. 25, No. 18, 5687, 2025.

[9] Yu, J. S. and L. J. Peters, "Measurement of constitutive parameters using the Mie solution of a scattering sphere," *Proceedings of the IEEE*, Vol. 58, No. 6, 876–885, 1970.

[10] Abbato, R., "Dielectric constant measurements using RCS data," *Proceedings of the IEEE*, Vol. 53, No. 8, 1095–1097, 1965.

[11] Eyraud, C., J.-M. Geffrin, A. Litman, and H. Tortel, "Complex permittivity determination from far-field scattering patterns," *IEEE Antennas and Wireless Propagation Letters*, Vol. 14, 309–312, 2015.

[12] Bohren, C. F. and D. R. Huffman, *Absorption and Scattering of Light by Small Particles*, John Wiley & Sons, 1983.

[13] Eyraud, C., J.-M. Geffrin, A. Litman, P. Sabouroux, and H. Giovannini, "Drift correction for scattering measurements," *Applied Physics Letters*, Vol. 89, No. 24, 244104, 2006.

[14] Taylor, J. R., *An Introduction to Error Analysis: The Study of Uncertainties in Physical Measurements*, University Science Books, 1997.

[15] Baker-Jarvis, J., M. D. Janezic, B. Riddle, C. L. Holloway, N. G. Paulter, and J. E. Blendell, "Dielectric and conductor-loss characterization and measurements on electronic packaging materials," Technical Note 1520, National Institute of Standards and Technology (NIST), 2001.

[16] Riddle, B., J. Baker-Jarvis, and J. Krupka, "Complex permittivity measurements of common plastics over variable temperatures," *IEEE Transactions on Microwave Theory and Techniques*, Vol. 51, No. 3, 727–733, 2003.